Spin-Dependent Dynamics of Photocarrier Generation in Electrically Detected Nitrogen-Vacancy-Based Quantum Sensing

Hiroki Morishita,[1,2,*,‡] Naoya Morioka,[1,2] Testuri Nishikawa,[1,3] Hajime Yao,[1,3] Shinobu Onoda,[4] Hiroshi Abe,[4] Takeshi Ohshima,[4] and Norikazu Mizuochi[1,2,†]

[1] *Institute for Chemical Research, Kyoto University, Gokasho, Uji, Kyoto 611-0011, Japan*

[2] *Center for Spintronics Research Network, Institute for Chemical Research, Kyoto University, Gokasho, Uji, Kyoto 611-0011, Japan*

[3] *Department of Molecular Engineering, Graduate School of Engineering, Kyoto University, Nishikyo-Ku, Kyoto 615-8510, Japan*

[4] *National Institutes for Quantum Science and Technology, Takasaki, Gunma 370-1292, Japan*

(Received 21 October 2022; accepted 16 February 2023; published 20 March 2023)

Electrical detection of nitrogen-vacancy (N-V) centers in diamond is advantageous for developing and integrating quantum information processing devices and quantum sensors and has the potential to achieve a higher collection efficiency than that of optical techniques. However, the mechanism for the electrical detection of N-V spins is not fully understood. In this study, we observe positive contrast in photocurrent detected magnetic resonance (PDMR). Note that negative PDMR contrast is usually observed. To discuss the sign of the PDMR contrast, we numerically analyze the dynamics of photocarrier generation by N-V centers using a seven-level rate model. It is found that the sign of the PDMR contrast depends on the difference in the photocurrent generated from the excited states and the metastable state of N-V centers. Furthermore, we demonstrate ac magnetic field sensing using spin coherence with the PDMR technique. ac magnetic field measurement with the PDMR technique is still challenging because the noise from a fluctuating magnetic environment is greater than the measured signal. Here, we introduce noise suppression using a phase-cycling-based noise-canceling technique. We demonstrate electrically detected ac magnetic field sensing with a sensitivity of 29 nT $Hz^{-1/2}$. Finally, we discuss sensitivity enhancement based on the proposed model.

DOI: 10.1103/PhysRevApplied.19.034061

I. INTRODUCTION

Nitrogen-vacancy (N-V) centers in diamond are promising candidates for room-temperature quantum sensors due to their long electron-spin coherence under ambient conditions [1–4]. N-V-based quantum sensors can be used in applications, such as biosensors [5–7], nanoscale nuclear magnetic resonance [8–11], and nuclear magnetic resonance imaging [12–14]. In previous demonstrations, the N-V electron spin was detected optically. Another method, called photocurrent detected magnetic resonance (PDMR), has attracted attention. The PDMR technique can read out the N-V electron spin [15–19] and coupled nuclear spins [20,21]. Electrical detection is expected to achieve a higher collection efficiency than that of optical techniques by optimizing the electrode structure [18]. For optical detection techniques, the photon collection efficiency is inherently limited by the high refractive index of diamond. In addition, the electrical detection technique is particularly advantageous for developing and integrating quantum sensors and other quantum devices [20,22]. Nevertheless, there has been no demonstration of electrically detected N-V-based quantum sensing using spin coherence controlled by microwave (MW) pulses, which corresponds to quantum coherence defined by Degen *et al.* [2] to describe the quantum sensor. Although electrically detected MW-free sensing [22] and dc magnetic field sensing with the continuous-wave PDMR technique [23] have been reported, a method that combines electrical readout and pulse control is difficult to implement because electrical detection is susceptible to noise currents from fluctuating magnetic field environments. By applying a phase-cycling-based noise-canceling technique [24] to suppress the noise current induced by a fluctuating magnetic environment, in this study, we demonstrate the electrical detection of

*hiroki.morishita.d8@tohoku.ac.jp

†mizuochi@scl.kyoto-u.ac.jp

‡Present addresses: Center for Spintronics Research Network, Tohoku University, Sendai, Miyagi, 980-8577 Japan. Advanced Institute for Materials Research, Tohoku University, Sendai, Miyagi, 980-8577 Japan.

an ac magnetic field using N-V electron-spin coherence. Furthermore, we report the observation of the positive PDMR contrast, which is unambiguously determined using a time-resolved current detection technique. We discuss the PDMR mechanism based on the observed positive contrast and the outlook for the enhancement of the sensitivity of N-V-based quantum sensors.

The PDMR signal of N-V centers is a spin-dependent photocurrent change resulting from the charge-state conversion between N-V^- and N-V^0 [15–22,25–28]. The photocarriers (electrons and holes) are generated under 532-nm laser illumination following the steps illustrated in Fig. 1(a). The first step is the excitation from the $^3A_2$ ground state to the ^3E excited state of N-V^- followed by electron ionization to the conduction band. There are two possible ionization pathways [15,26,28]: from the triplet ^3E state shown in Fig. 1(a, I, i) and from the singlet ^1E state after intersystem crossing shown in Fig. 1(a, I, ii). The ionization changes the N-V charge state to N-V^0. Next, N-V^0 is excited from the ^2E ground state to the $^2A_2$ excited state and subsequently photoionized to N-V^- by emitting a hole into the valence band [Fig. 1(a, II)]. The electron and hole act as photocarriers and are detected as an electric current in PDMR. The spin-dependent photocurrent originates from a higher transition probability of $|\pm1\rangle$ in the N-V^- ^3E excited state to the $^1A_1$ singlet state. The application of resonant MWs to the initialized electron spin state $|0\rangle$ either decreases or increases the photocurrent when the N-V^- electron is ionized from the triplet ^3E [Fig. 1(a, I, i)] or the singlet ^1E [Fig. 1(a, I, ii)], respectively. Thus, the sign of the PDMR signal depends on the electron ionization path. We discuss the dominant pathway later.

II. EXPERIMENTS

The sample used in this study is a high-pressure high-temperature synthesized diamond that contains an ensemble of N-V centers with a concentration of approximately 1.4×10^{17} cm^{-3}. The N-V centers are created by 2-MeV electron irradiation with a fluence of 1×10^{17} cm^{-2} at 745 °C, followed by annealing at 1000 °C for 1 h in an argon atmosphere. Interdigital electrodes with the structure

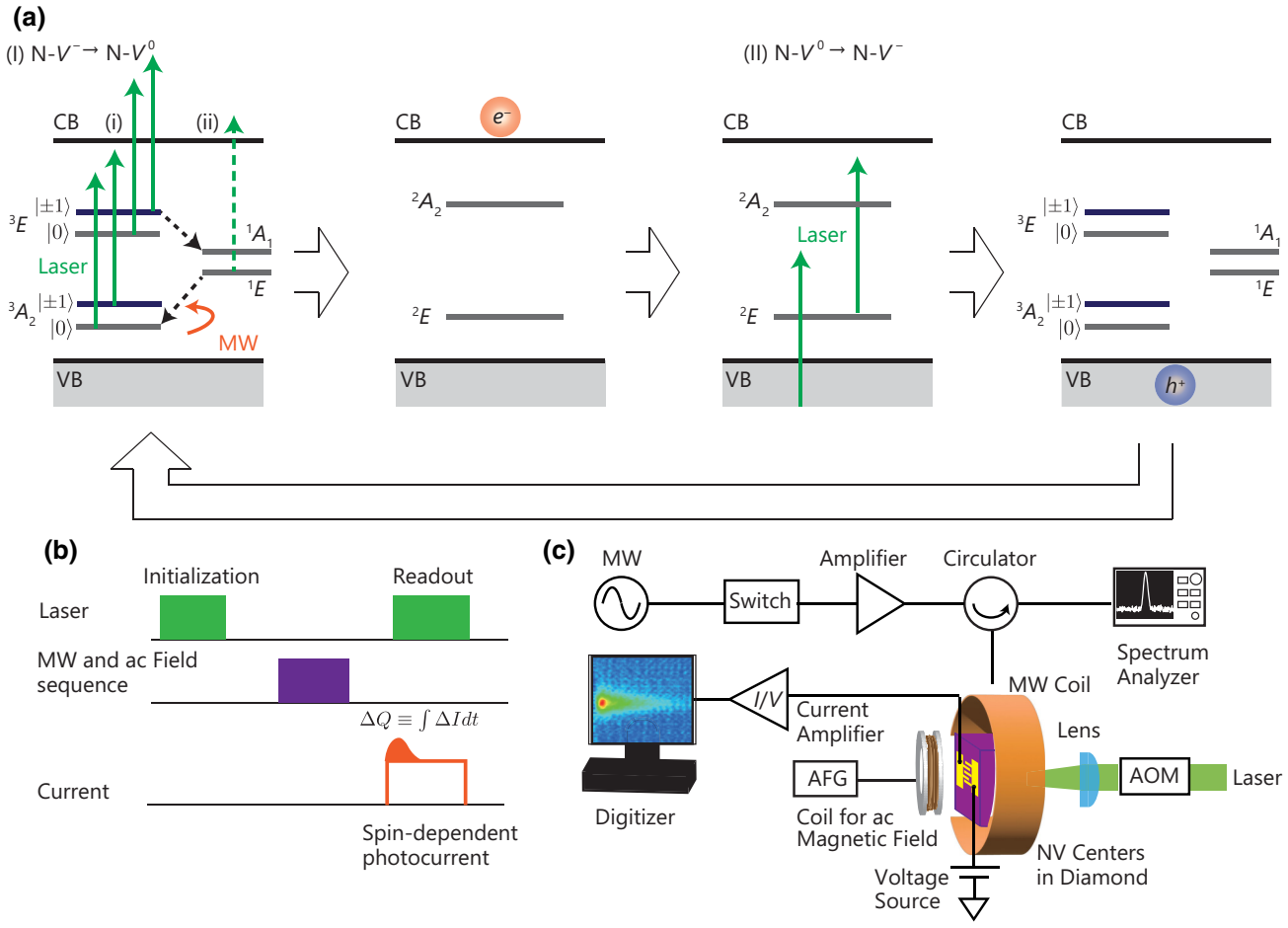

FIG. 1. (a) Schematic diagram of PDMR measurement of N-V^- center. Photoexcited carriers are generated under 532-nm laser illumination [processes shown in (I–II)]. Process (I) includes a reported ionization path [solid arrow, (i)] and a proposed ionization path [dashed arrow, (ii)]. (b) Process of PDMR measurements. (c) Schematic diagram of PDMR spectrometer.

Au(100 nm)/Pt(5 nm)/Ti(30 nm) are fabricated on the diamond surface for electrical spin detection. The distance between electrodes is approximately 10 μm.

We use the home-built PDMR spectrometer shown in Fig. 1(c). MW pulses are applied to the N-V centers with a single-turn coil with a resonance frequency of approximately 2.87 GHz. A 532-nm laser illuminated the sample through a lens with a focal length of 100 mm (spot size of approximately 1×10^5 μm^2) to initialize N-V electron spin and generate photocarriers from the N-V centers. The time transient of the photocurrent is measured using a digitizer at 100 MSa s^{-1} through a current amplifier at a constant bias voltage. In the home-built PDMR spectrometer, the sign of the PDMR contrast is unambiguously defined using the digitizer instead of a lock-in amplifier. A coil connected to an arbitrary waveform generator (AFG) is used to generate a test ac magnetic field.

We use the pulse sequence shown in Fig. 1(b) to measure the transient of the photocurrent at an applied bias of 5 V without an external magnetic field. After the N-V electron spins are initialized by the first laser pulse, the MW sequence is applied to control the electron spin for various measurements, including pulsed PDMR and the coherence time (T_2) of the N-V electron spins. In ac magnetic field sensing, the MW and ac field sequence is applied. Finally, the laser pulse illuminated the N-V centers to generate photocarriers. In this study, we choose a laser pulse length of 50 μs and a MW power of approximately 250 mW (π pulse width: 110 to 140 ns). The PDMR signal intensity (ΔQ), with units of coulombs (C), is defined as ΔI integrated over the time during which the photocurrent was changing $\left(\Delta Q \equiv \int \Delta I dt\right)$ [20], where ΔI is the difference between the detected photocurrent with on-resonance MW pulses and that with off-resonance or no MW pulses, as shown in Fig. 1(b).

III. RESULTS AND DISCUSSION

First, we measure the resonance frequency and the contrast of the PDMR signal using a pulsed PDMR technique with the pulse sequence shown in Fig. 2(a) with a sweeping MW frequency. Figure 2(b) shows ΔQ as a function of the MW frequency obtained from the pulsed PDMR measurement. The squares and the solid red line correspond to the experimental data and the curve-fitting results obtained using a Lorentzian function, respectively. We obtain a resonance frequency of approximately 2.87 GHz and a positive signal contrast of approximately 5%. The observed resonance frequency is in good agreement with a N-V center's zero-field splitting [29], which confirms that we observe the PDMR signal of the N-V centers with the pulsed PDMR technique.

To discuss the PDMR mechanism, we measure the laser power dependence of the pulsed PDMR peak area. Figure 2(d) shows the pulsed PDMR peak area (black squares) and the total photocurrent generated by the pulse sequence shown in Fig. 2(c) (dots) as a function of the laser power. The total photocurrent (I) can be expressed as

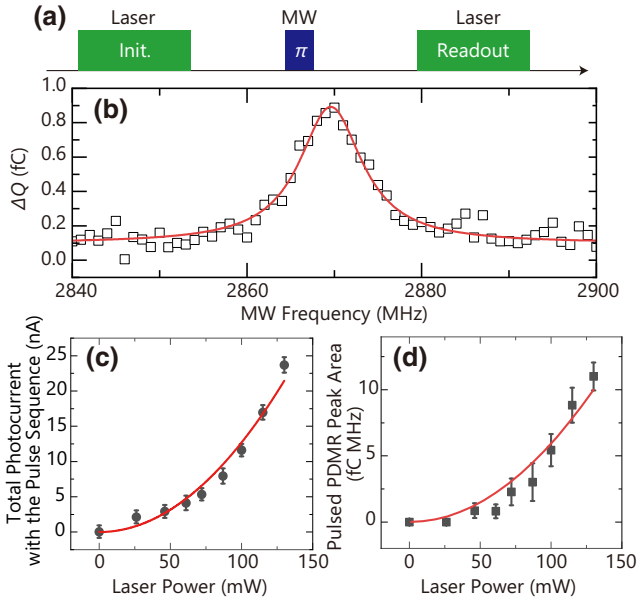

FIG. 2. (a) Pulse sequence used to measure pulsed PDMR spectrum. (b) Pulsed PDMR spectrum of ensemble of N-V centers without external magnetic field. (c) Total photocurrent obtained with pulse sequence shown in (a). Dots and solid line are the experimental data and fitting results, respectively. (d) Pulsed PDMR peak area as a function of laser power. Squares and solid line are the experimental data and the simulation results obtained using the seven-level rate model, respectively.

$$I = \frac{\alpha\beta P^2}{1+\beta P} + bP, \tag{1}$$

where α, β, and $b \geq 0$ are fitting parameters, and P is the laser power [27,30]. The first term represents the photocurrent generated from the N-V centers via the two-photon process. It shows a quadratic dependence on the laser power because of the two-photon ionization mechanism when the laser power is sufficiently weak ($\beta P \ll 1$) to not saturate the excitation from the $^3A_2$ ground state to the ^3E excited state. In this regime, the photocurrent from the N-V center can be well described by $I \approx aP^2$. At higher laser powers ($\beta P \gg 1$), the power dependence of the photocurrent from the N-V center becomes linear due to the saturation of the excitation from the $^3A_2$ ground state to the ^3E excited state. The second term represents the background photocurrent from other defects via the one-photon ionization process. The total photocurrent can be fitted using the quadratic function $I = aP^2 + bP$ with $a = 1.2$ pA mW^{-2}, $b = 0$ pA mW^{-1}, and the constraints a, $b \geq 0$ [solid red line in Fig. 2(c)]. Thus, the excitation of the N-V center from the $^3A_2$ ground state to the ^3E excited

state is not saturated. In addition, the one-photon contribution is below the noise level and is negligibly small, which is different from the results in previous PDMR studies [15,30], where about 10%–20% of the total photocurrent is attributed to the one-photon process. Figure 2(d) shows that the pulsed PDMR peak area quadratically increases with laser power and that the pulsed PDMR signals have a positive sign, opposite to that for the optically detected magnetic resonance (ODMR) contrast. Recently, Bourgeois *et al*. [30] also observed a positive PDMR contrast. They argued that while they basically observed a negative PDMR contrast due to the triplet ionization pathway, the sign of the PDMR contrast was reversed due to the one-photon process of acceptor impurities. Since we did not observe the one-photon contribution to the photocurrent [see Fig. 2(c)], we attribute the positive PDMR contrast to the ionization mechanism, i.e., ionization from the singlet ^1E level is the dominant pathway shown in Fig. 1(a, I, ii).

To further elucidate the excitation dynamics, we analyze a seven-level rate model considering spin and charge-state conversion dynamics, as shown in Fig. 3(a). We denote $m_s = 0$ and $m_s = \pm 1$ in the ground and (excited) states of N-V^- as $|1\rangle$ and $|2\rangle$ ($|3\rangle$ and $|4\rangle$), respectively. $|5\rangle$ is the metastable singlet state of N-V^-. $|6\rangle$ and $|7\rangle$ are the ground and excited states of N-V^0, respectively. We denote the transition rate from $|n\rangle$ to $|m\rangle$ as k_{nm}. These rates include spontaneous decay and laser-induced transitions. We assume that the rates of laser-induced transitions are proportional to the laser power P, i.e., $k_{nm} = \gamma_{nm}P$. We define the coefficients of the laser-excitation rates from $|1\rangle$ to $|3\rangle$ and from $|2\rangle$ to $|4\rangle$ as $\gamma_{13} = \gamma_{24} = a_n$. The laser-excitation rate from $|6\rangle$ to $|7\rangle$ has been reported to be $\gamma_{67} = 1.3a_n$ [31]. In this model, an electron in the conduction band is generated via the laser-excited ionization process from N-V^- and N-V^0. The triplet ionization rate from either $|3\rangle$ or $|4\rangle$ to $|6\rangle$ has been reported to be $\gamma_{36} = \gamma_{46} = 0.037a_n$ [31]. A hole in the valence band is emitted with the charge-state recovery process from N-V^0 to N-V^- with laser excitation. The charge-state recovery rate from $|7\rangle$ to either $|1\rangle$ or $|2\rangle$ has been reported to be $\gamma_{71} = \gamma_{72} = 0.08a_n$ [31]. Other reported values of the spontaneous transition rates are summarized in Fig. 3(a) [32,33]. Furthermore, this model includes charge-state conversion between N-V^- and N-V^0 in the dark. The dark ionization (d_i) rate from either $|1\rangle$ or $|2\rangle$ to $|6\rangle$ has been reported to be $k_{16} = k_{26} = d_i = (100\ \mu\text{s})^{-1}$ [34]. The dark recovery rate (d_r) from $|6\rangle$ to either $|1\rangle$ or $|2\rangle$ of $k_{61} = k_{62} = d_r = 2.7d_i$ is estimated according to the charge-state ratio N-V^-: N-V^0 $\sim$ 7:3 with 532-nm laser excitation [35]. The unknown parameters are a_n and the singlet ionization rate from $|5\rangle$ to $|6\rangle$ (γ_{56}). We numerically analyze them by solving the model using the pulse sequence shown in Fig. 2(a). From the population dynamics under the readout laser, we calculate the pulsed PDMR peak area using the following relation:

$$\text{pulsed PDMR peak area} \propto \int (\gamma_{36}\, p_{|3\rangle}(t) + \gamma_{46}\, p_{|4\rangle}(t) + \gamma_{56}\, p_{|5\rangle}(t))P\, dt, \quad (2)$$

where $p_{|n\rangle}(t)$ is the population of $|n\rangle$ as a function of time. Here, we choose the same integration time as that used in the experiments. When we set $a_n = 1.1 \times 10^{-3}$ W^{-1} ns^{-1} and $\gamma_{56} = 4.4 \times 10^{-3}\, a_n$, we reproduce the results for the laser power dependence of the pulsed PDMR contrast and the pulsed PDMR peak area with a positive scaling factor [the solid line in Fig. 2(d)]. The observed a_n is close to the theoretical estimate of 2.2×10^{-3} W^{-1} ns^{-1} obtained using the spot size and the N-V^- absorption cross section [36]. The ratio $\gamma_{36}(\gamma_{46})/\gamma_{56} \sim 0.1$ is similar to that reported in a theoretical study [28]. Since the lifetime of $|5\rangle$ is longer than those of $|3\rangle$ and $|4\rangle$, the singlet ionization probability is higher than that for triplet ionization even with the low singlet ionization rate. Thus, the singlet ionization pathway can be involved in the excitation dynamics in the PDMR measurement, as is the ionization from the triplet excited states.

Next, we discuss the PDMR contrast sign in more detail using the numerical simulation results. Figure 3(b) shows ΔI, which is the difference in photocurrent with and without the MW pulse, as a function of time after the laser illumination was turned on (t_{laser}) for a laser power density of 1.2×10^2 W cm^{-2}. The black, red, and blue curves in Fig. 3(b) show the sum of ΔI generated from the excited states $|3\rangle$ and $|4\rangle$ (ΔI_{34}), ΔI generated from the singlet metastable state $|5\rangle$ (ΔI_5), and the sum of ΔI generated from $|3\rangle$, $|4\rangle$, and $|5\rangle$ (ΔI_{345}), respectively. Figure 3(b) shows that ΔI_{34} is negative and ΔI_5 is positive at any t_{laser}. On the other hand, the sign of the total photocurrent ΔI_{345} is time dependent; ΔI_{345} is negative (positive) at $t_{\text{laser}} < (>)$ $\sim$250 ns. This sign change occurs because $|\Delta I_5|$ is larger than $|\Delta I_{34}|$ at $t_{\text{laser}} \gtrsim 250$ ns. Since the sign of ΔI_{345} depends on t_{laser}, the PDMR contrast depends on the integration time window. Here, we plot the PDMR contrast as a function of laser power density and k_{46}/k_{45} for six different integration times [Fig. 3(c)]. We find that an integration time of below approximately 600 ns gives a negative PDMR contrast regardless of the laser power density. When the integration time is longer than approximately 600 ns, the sign of the PDMR contrast depends on the laser power density. The positive PDMR contrast increases with increasing laser power density. The maximum positive contrast is observed for a laser power density of approximately 1×10^2 W cm^{-2} at an integration time of 5 μs. When the laser power density is above approximately 1×10^2 W cm^{-2}, the positive contrast worsens because $|\Delta I_{34}|$ increases within the short lifetime of the excited states. When ΔI_{34} is dominant, the sign of the PDMR contrast is negative. Previous studies [16–18] reported a

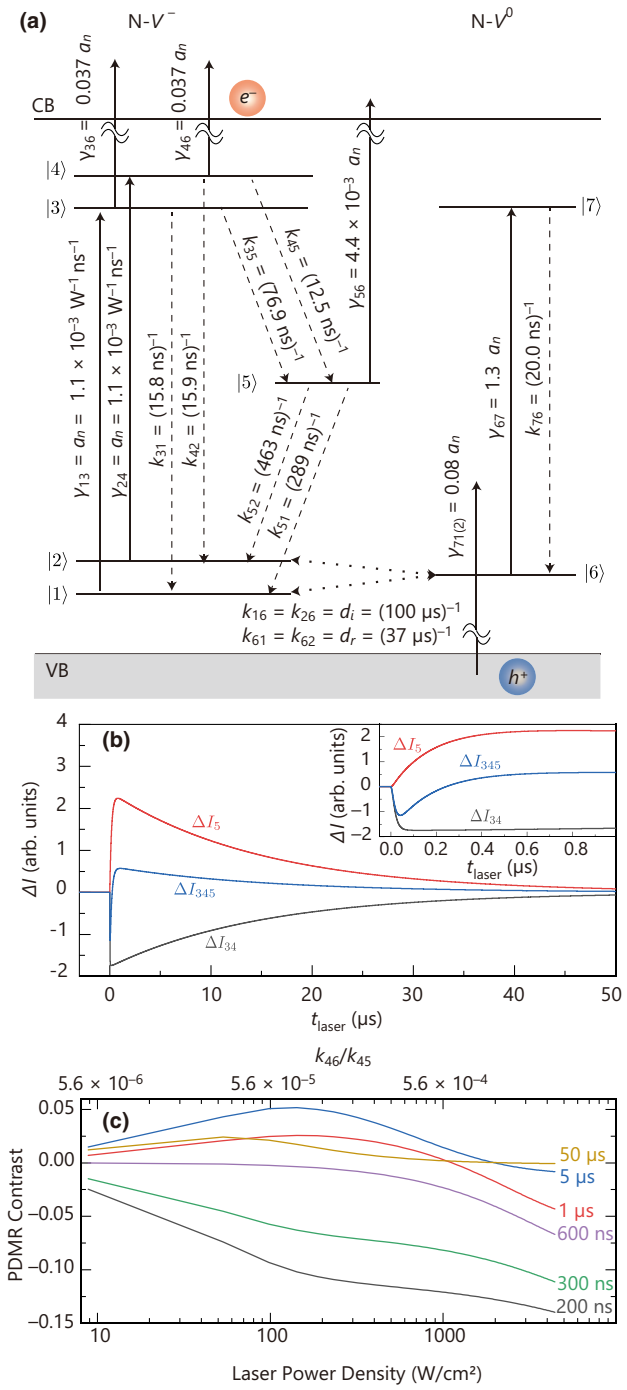

FIG. 3. (a) Proposed seven-level rate model considering spin and charge-state conversion dynamics. The solid, broken, and dotted arrows show the laser-excitation rate, spontaneous decay, and charge-state conversion in the dark, respectively. (b) Difference in photocurrent with and without on-resonance MW pulse (ΔI) as a function of time after the laser is turned on (t_{laser}). The black, red, and blue curves show the sum of ΔI generated from the excited states $|3\rangle$ and $|4\rangle$ (ΔI_{34}), ΔI generated from the metastable state $|5\rangle$ (ΔI_5), and the sum of ΔI generated from $|3\rangle$, $|4\rangle$, and $|5\rangle$ (ΔI_{345}), respectively. (c) PDMR contrast as function of laser power density and k_{46}/k_{45} for six integration times (200 ns, 300 ns, 600 ns, 1 μs, 5 μs, and 50 μs).

negative PDMR contrast because the pulsed PDMR experiments are performed using a short laser pulse duration (<1 μs) and high-power laser excitation such that two-photon excitation from the excited states is dominant. In contrast, we use a long-laser duration of 50 μs with a 5-μs integration time and a low laser power density of 1.2×10^2 W cm^{-2}. As a result, the observed PDMR signals have a positive sign. We note that because we use a transimpedance amplifier with a 10^7-V A^{-1} gain and a 1-MHz bandwidth, a negative PDMR signal ($\lesssim$ 600 ns) could not be detected under the present experimental conditions.

Since the sensitivity of the ac magnetic field sensing is proportional to $1/\sqrt{T_2}$, we measure T_2 and compare it to that obtained using ODMR to show that electrical detection does not deteriorate T_2. Figure 4(a) shows the pulse sequence used for the electrical T_2 measurements. Here, we measure ΔQ as a function of the total free evolution time (2τ). $\pm x$ in the MW pulses show the MW phase. We use the phase-cycling technique to remove MW-induced artifact noise and common-mode noise [20]. The ΔQ for the electrical T_2 measurement is plotted on the vertical axis of Fig. 4(b) as the difference between ΔQ with the $(\pi/2)_{+x} - (\pi)_{+x} - (\pi/2)_{-x}$ sequence and ΔQ with the $(\pi/2)_{+x} - (\pi)_{+x} - (\pi/2)_{+x}$ sequence, where the subscripts $\pm x$ show the MW phase. We observe stretched exponential

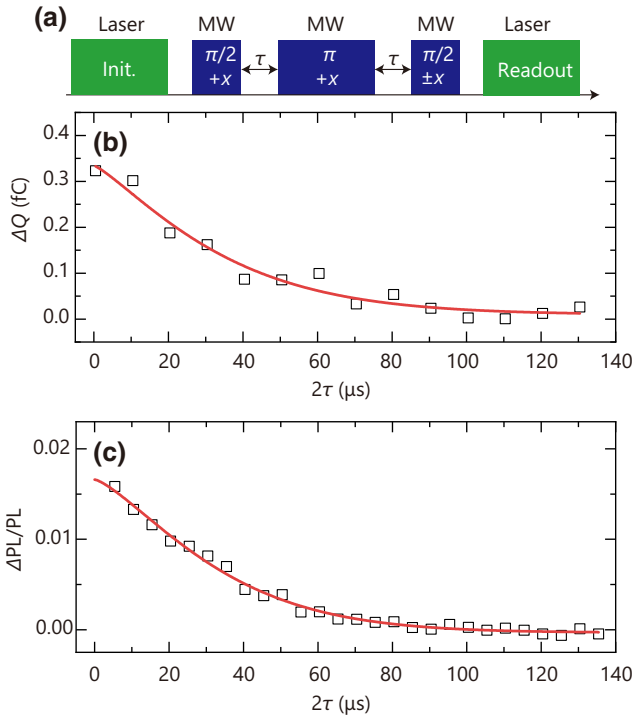

FIG. 4. (a) Pulse sequence used to measure T_2. $\pm x$ indicate the phase of MW pulses. (b) Echo decay shown in ΔQ as a function of 2τ. The experimental data (squares) are fitted to a stretched exponential decay function (solid red line). (c) Echo decay shown in ΔPL/PL as a function of 2τ.

decay (a stretching parameter of 1.2 ± 0.3) with $T_2 \sim 37$ μs, which is very close to the value $T_2 \sim 36$ μs separately determined using the home-built confocal microscope setup [Fig. 4(c)]. These results indicate that the possible charge noise caused by ionization and the detection method do not affect spin coherence.

Next, we demonstrate ac magnetic field sensing with the electrical technique using the pulse sequence shown in Fig. 5(a). In this sequence, a Hahn-echo sequence $(\pi/2)_{+x} - (\pi)_{+x} - (\pi/2)_{+y}$ is applied, which is synchronized with the target ac magnetic field $B(t) = B_{\rm ac}\cos(2\pi f_{\rm ac})$, where $B_{\rm ac}$ and $f_{\rm ac}$ are amplitude and frequency of the ac magnetic field, respectively [1–3]. During the free evolution time of $2\tau \sim f_{\rm ac}^{-1}$, the spin accumulates the phase $\phi \propto B_{\rm ac}\tau$ from the alternating field [1–3], which is projected to S_z with the last $(\pi/2)_y$ pulse to readout the phase through the photocurrent oscillating by $\sin\phi$. The phase of the last $(\pi/2)_y$ pulse can be inverted as $(\pi/2)_{-y}$ to obtain a signal with the opposite sign. We measure ΔQ as a function of the amplitude of the test ac magnetic field ($B_{\rm ac}$). Here, we set τ at $T_2/4$ [3,37] and detected the ac magnetic field oscillating at $f_{\rm ac} =$ 46 kHz. The phases of the MW pulses show a subscript of x or $\pm y$ in Fig. 5(a). Figures 5(b) and 5(c) show the results for ac magnetic field sensing with electrical detection using the pulse sequences $(\pi/2)_{+x} - (\pi)_{+x} - (\pi/2)_{+y}$ and $(\pi/2)_{+x} - (\pi)_{+x} - (\pi/2)_{-y}$, respectively. They show that background noise increases with $B_{\rm ac}$ when the pulse sequences $(\pi/2)_{+x} - (\pi)_{+x} - (\pi/2)_{+y}$ and $(\pi/2)_{+x} - (\pi)_{+x} - (\pi/2)_{-y}$ are separately applied. This noise is due to the induced current due to the integration of the ac coil. To suppress the background noise, we use the phase-cycling-based noise-canceling technique [24], as shown in Fig. 5(d). This sequence is the alternating application of the pulse sequences $(\pi/2)_{+x} - (\pi)_{+x} - (\pi/2)_{+y}$ and $(\pi/2)_{+x} - (\pi)_{+x} - (\pi/2)_{-y}$. Because this pulse sequence can suppress frequencies other than the odd-harmonic components of $f_{\rm mod}$ (approximately 5.8 kHz) [24], the induced current with a frequency of approximately 46 kHz can be suppressed. Figure 5(e) shows the results for ac magnetic field sensing using the noise-canceling technique with a baseline correction. We observe the oscillation of ΔQ as a function of $B_{\rm ac}$. The solid line shows the curve fitting results obtained using a damped sinusoidal function. Using the results for the curve fitting, the minimum detectable magnetic field ($\delta B_{\rm min}$) can be calculated as $\delta B_{\rm min} = \sigma / \max|d\Delta Q/dB_{\rm ac}|$, where σ is the standard deviation of the intensity of Hahn-echo measurements. Next, we measure the dependence of $\delta B_{\rm min}$ on the measurement time (T) shown in Fig. 5(f). The solid red line in Fig. 5(f) shows the curve-fitting results obtained using the relation $\delta B_{\rm min} = \eta/\sqrt{T}$ [1]. The observed data can be fitted well by the relation. We obtain a sensitivity of approximately 29 ± 1 nT Hz$^{-1/2}$ and a minimum detectable magnetic field of approximately 16 nT for an approximately 7-s measurement.

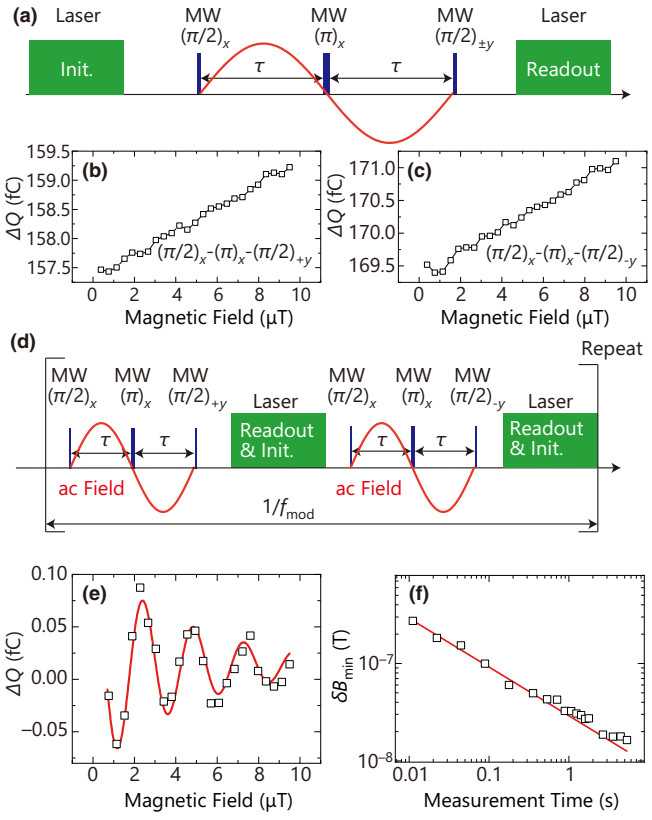

FIG. 5. (a) Pulse sequence for ac magnetic field sensing with electrical detection. Results for ac magnetic field sensing obtained using pulse sequence (b) $(\pi/2)_{+x} - (\pi)_{+x} - (\pi/2)_{+y}$ and (c) $(\pi/2)_{+x} - (\pi)_{+x} - (\pi/2)_{-y}$. (d) Pulse sequence for ac magnetic field sensing with phase-cycling-based noise-canceling technique. (e) Results for ac magnetic field sensing with phase-cycling-based noise-canceling technique. (f) $\delta B_{\rm min}$ as a function of measurement time (T).

Finally, we discuss the electrically detected ac magnetic field sensitivity ($\eta_{\rm ac}$) of the N-V-based magnetometer using the proposed ionization model [see Fig. 3(a)]. To compare the sensitivity of PDMR to that of ODMR, we use shot-noise-limited $\eta_{\rm ac}$, which can be expressed as [23]

$$\eta_{\rm ac} \propto \frac{1}{|c|\sqrt{NT_2}}, \tag{3}$$

where c and N are the contrast of a PDMR or ODMR signal and the number of N-V spins, respectively. Here, we assume that current shot noise is negligibly small. Although we observe almost the same T_2 with electrical and optical detection, the 5% PDMR contrast is much lower than the approximately 30% ODMR contrast obtained from the proposed model. However, we can enhance the PDMR contrast, e.g., by using excitation at other wavelengths. For example, the ratio $\gamma_{36}(\gamma_{46})/\gamma_{56}$ becomes approximately 0.3 for a 766-nm laser [31]. This

ratio is 3 times higher than that at 532 nm. For this longer wavelength, the maximum PDMR contrast is approximately 0.3. In this situation, PDMR has the potential to have a sensitivity that is comparable to that of the optical technique. This study also use the phase-cycling-based noise-canceling technique to measure the ac magnetic field, but the odd-harmonic components of f_{mod} cannot be suppressed by this technique. More suppression of the noise current induced by the fluctuating magnetic environment is needed to improve the sensitivity (e.g., by designing a filter function) [2]. Thus, selecting the appropriate excitation wavelength and designing a filter function will enhance the sensitivity of the N-V-based magnetometer with the electrical detection technique.

IV. CONCLUSION

In conclusion, we observe a positive PDMR contrast and numerically analyze a seven-level rate model to discuss the sign of the PDMR contrast. The numerical simulation results show that the PDMR signal has a positive contrast when ΔI_5 becomes dominant at a low-laser power density and a long integration time ($\gtrsim$600 ns) is used. We demonstrate ac magnetic field sensing using a N-V-based quantum sensor with the electrical spin-coherence detection technique. In the ac magnetic sensing demonstration, the fluctuating magnetic-environment-induced current noise, which affects sensing. To suppress such noise, we use a phase-cycling-based noise-canceling technique. With this technique, we obtain a sensitivity of η_{ac} $\sim$29 nT Hz$^{-1/2}$. Furthermore, we discuss the enhancement of the sensitivity of the N-V-based magnetometer with electrical detection. The proposed technique can be applied to measure ac and dc magnetic fields, electric fields, and temperature, and is readily applicable for conventional electrical detection with a lock-in amplifier.

ACKNOWLEDGMENTS

We thank T. Ono, T. Moriyama, and Y. Shiota for their technical help. This work is supported by the Ministry of Education, Culture, Sports, Science and Technology (MEXT) of Japan under the Quantum Leap Flagship Program (Q-LEAP) (Grant No. JPMXS0118067395), the Japan Society for the Promotion of Science (JSPS) KAKENHI (Grant No. 19H02546), and the Kyoto University Nano Technology Hub in the Advanced Research Infrastructure for Materials and Nanotechnology Project sponsored by MEXT.

[1] J. M. Taylor, P. Cappellaro, L. Childress, L. Jiang, D. Budker, P. R. Hemmer, A. Yacoby, R. Walsworth, and M. D. Lukin, High-sensitivity diamond magnetometer with nanoscale resolution, Nat. Phys. **4**, 810 (2008).

[2] C. L. Degen, F. Reinhard, and P. Cappellaro, Quantum sensing, Rev. Mod. Phys. **89**, 035002 (2017).

[3] E. D. Herbschleb, H. Kato, Y. Maruyama, T. Danjo, T. Makino, S. Yamasaki, I. Ohki, K. Hayashi, H. Morishita, M. Fujiwara, and N. Mizuochi, Ultra-long coherence times amongst room-temperature solid-state spins, Nat. Commun. **10**, 3766 (2019).

[4] J. F. Barry, J. M. Schloss, E. Bauch, M. J. Turner, C. A. Hart, L. M. Pham, and R. L. Walsworth, Sensitivity optimization for NV-diamond magnetometry, Rev. Mod. Phys. **92**, 015004 (2020).

[5] F. Shi, F. Kong, P. Zhao, X. Zhang, M. Chen, S. Chen, Q. Zhang, M. Wang, X. Ye, Z. Wang, *et al.*, Single-DNA electron spin resonance spectroscopy in aqueous solutions, Nat. Methods **15**, 697 (2018).

[6] R. W. de Gille, J. M. McCoey, L. T. Hall, J. P. Tetienne, E. P. Malkemper, D. A. Keays, L. C. L. Hollenberg, and D. A. Simpson, Quantum magnetic imaging of iron organelles within the pigeon cochlea, Proc. Natl. Acad. Sci. U. S. A. **118**, e2112749118 (2021).

[7] S. Sotoma, C. Zhong, Y. Kah James Chen, H. Yamashita, T. Plakhotnik, Y. Harada, and M. Suzuki, In situ measurements of intracellular thermal conductivity using heater-thermometer hybrid diamond nanosensors, Sci. Adv. **7**, eabd7888 (2021).

[8] N. Aslam, M. Pfender, P. Neumann, R. Reuter, A. Zappe, F. Favaro de Oliveira, A. Denisenko, H. Sumiya, S. Onoda, J. Isoya, and J. Wrachtrup, Nanoscale nuclear magnetic resonance with chemical resolution, Science **357**, 67 (2017).

[9] D. R. Glenn, D. B. Bucher, J. Lee, M. D. Lukin, H. Park, and R. L. Walsworth, High-resolution magnetic resonance spectroscopy using a solid-state spin sensor, Nature **555**, 351 (2018).

[10] D. B. Bucher, D. R. Glenn, H. Park, M. D. Lukin, and R. L. Walsworth, Hyperpolarization-Enhanced NMR Spectroscopy with Femtomole Sensitivity Using Quantum Defects in Diamond, Phys. Rev. X **10**, 021053 (2020).

[11] N. Arunkumar, D. B. Bucher, M. J. Turner, P. TomHon, D. Glenn, S. Lehmkuhl, M. D. Lukin, H. Park, M. S. Rosen, T. Theis, and R. L. Walsworth, Micron-Scale NV-NMR Spectroscopy with Signal Amplification by Reversible Exchange, PRX Quantum **2**, 010305 (2021).

[12] D. Rugar, H. J. Mamin, M. H. Sherwood, M. Kim, C. T. Rettner, K. Ohno, and D. D. Awschalom, Proton magnetic resonance imaging using a nitrogen-vacancy spin sensor, Nat. Nanotechnol. **10**, 120 (2015).

[13] S. J. DeVience, L. M. Pham, I. Lovchinsky, A. O. Sushkov, N. Bar-Gill, C. Belthangady, F. Casola, M. Corbett, H. Zhang, M. Lukin, *et al.*, Nanoscale NMR spectroscopy and imaging of multiple nuclear species, Nat. Nanotechnol. **10**, 129 (2015).

[14] V. S. Perunicic, C. D. Hill, L. T. Hall, and L. C. L. Hollenberg, A quantum spin-probe molecular microscope, Nat. Commun. **7**, 12667 (2016).

[15] E. Bourgeois, A. Jarmola, P. Siyushev, M. Gulka, J. Hruby, F. Jelezko, D. Budker, and M. Nesladek, Photoelectric detection of electron spin resonance of nitrogen-vacancy centres in diamond, Nat. Commun. **6**, 8577 (2015).

[16] M. Gulka, E. Bourgeois, J. Hruby, P. Siyushev, G. Wachter, F. Aumayr, P. R. Hemmer, A. Gali, F. Jelezko, M. Trupke, and M. Nesladek, Pulsed Photoelectric Coherent Manipulation and Detection of N−*V* Center Spins in Diamond, Phys. Rev. Appl. **7**, 044032 (2017).

[17] F. M. Hrubesch, G. Braunbeck, M. Stutzmann, F. Reinhard, and M. S. Brandt, Efficient Electrical Spin Readout of NV^- Centers in Diamond, Phys. Rev. Lett. **118**, 037601 (2017).

[18] P. Siyushev, M. Nesladek, E. Bourgeois, M. Gulka, J. Hruby, T. Yamamoto, M. Trupke, T. Teraji, J. Isoya, and F. Jelezko, Photoelectrical imaging and coherent spin-state readout of single nitrogen-vacancy centers in diamond, Science **363**, 728 (2019).

[19] T. Murooka, M. Shiigai, Y. Hironaka, T. Tsuji, B. Yang, T. M. Hoang, K. Suda, K. Mizuno, H. Kato, T. Makino, *et al.*, Photoelectrical detection of nitrogen-vacancy centers by utilizing diamond lateral p–i–n diodes, Appl. Phys. Lett. **118**, 253502 (2021).

[20] H. Morishita, S. Kobayashi, M. Fujiwara, H. Kato, T. Makino, S. Yamasaki, and N. Mizuochi, Room temperature electrically detected nuclear spin coherence of NV centres in diamond, Sci. Rep. **10**, 792 (2020).

[21] M. Gulka, D. Wirtitsch, V. Ivady, J. Vodnik, J. Hruby, G. Magchiels, E. Bourgeois, A. Gali, M. Trupke, and M. Nesladek, Room-temperature control and electrical readout of individual nitrogen-vacancy nuclear spins, Nat. Commun. **12**, 4421 (2021).

[22] H. Zheng, J. Hruby, E. Bourgeois, J. Soucek, P. Siyushev, F. Jelezko, A. Wickenbrock, M. Nesladek, and D. Budker, Electrical-Readout Microwave-Free Sensing with Diamond, Phys. Rev. Appl. **18**, 024079 (2022).

[23] J. Hruby, M. Gulka, M. Mongillo, I. P. Radu, M. V. Petrov, E. Bourgeois, and M. Nesladek, Magnetic field sensitivity of the photoelectrically read nitrogen-vacancy centers in diamond, Appl. Phys. Lett. **120**, 162402 (2022).

[24] F. Hoehne, L. Dreher, J. Behrends, M. Fehr, H. Huebl, K. Lips, A. Schnegg, M. Suckert, M. Stutzmann, and M. S. Brandt, Lock-in detection for pulsed electrically detected magnetic resonance, Rev. Sci. Instrum. **83**, 043907 (2012).

[25] H. Kato, M. Wolfer, C. Schreyvogel, M. Kunzer, W. Müller-Sebert, H. Obloh, S. Yamasak, and C. Nebel, Tunable light emission from nitrogen-vacancy centers in single crystal diamond PIN diodes, Appl. Phys. Lett. **102**, 151101 (2013).

[26] D. P. L. Aude Craik, P. Kehayias, A. S. Greenspon, X. Zhang, M. J. Turner, J. M. Schloss, E. Bauch, C. A. Hart, E. L. Hu, and R. L. Walsworth, Microwave-Assisted Spectroscopy Technique for Studying Charge State in Nitrogen-Vacancy Ensembles in Diamond, Phys. Rev. Appl. **14**, 014009 (2020).

[27] P. Siyushev, H. Pinto, M. Vörös, A. Gali, F. Jelezko, and J. Wrachtrup, Optically Controlled Switching of the Charge State of a Single Nitrogen-Vacancy Center in Diamond at Cryogenic Temperatures, Phys. Rev. Lett. **110**, 167402 (2013).

[28] L. Razinkovas, M. Maciaszek, F. Reinhard, M. W. Doherty, and A. Alkauskas, Photoionization of negatively charged NV centers in diamond: Theory and *ab initio* calculations, Phys. Rev. B **104**, 235301 (2021).

[29] M. W. Doherty, N. B. Manson, P. Delaney, F. Jelezko, J. Wrachtrup, and L. C. L. Hollenberg, The nitrogen-vacancy colour centre in diamond, Phys. Rep. **528**, 1 (2013).

[30] E. Bourgeois, J. Soucek, J. Hruby, M. Gulka, and M. Nesladek, Photoelectric detection of nitrogen-vacancy centers magnetic resonances in diamond: Role of charge exchanges with other optoelectrically active defects, Adv. Quantum Technol. **5**, 2100153 (2022).

[31] L. Hacquebard and L. Childress, Charge-state dynamics during excitation and depletion of the nitrogen-vacancy center in diamond, Phys. Rev. A **97**, 063408 (2018).

[32] L. Robledo, H. Bernien, T. v. d. Sar, and R. Hanson, Spin dynamics in the optical cycle of single nitrogen-vacancy centres in diamond, New J. Phys. **13**, 025013 (2011).

[33] E. Fraczek, V. G. Savitski, M. Dale, B. G. Breeze, P. Diggle, M. Markham, A. Bennett, H. Dhillon, M. E. Newton, and A. J. Kemp, Laser spectroscopy of NV^- and NV^0 colour centres in synthetic diamond, Opt. Mater. Express **7**, 2571 (2017).

[34] D. Bluvstein, Z. Zhang, C. A. McLellan, N. R. Williams, and A. C. B. Jayich, Extending the Quantum Coherence of a Near-Surface Qubit by Coherently Driving the Paramagnetic Surface Environment, Phys. Rev. Lett. **123**, 146804 (2019).

[35] N. Aslam, G. Waldherr, P. Neumann, F. Jelezko, and J. Wrachtrup, Photo-induced ionization dynamics of the nitrogen vacancy defect in diamond investigated by single-shot charge state detection, New J. Phys. **15**, 013064 (2013).

[36] R. Chapman and T. Plakhotnik, Anomalous saturation effects due to optical spin depolarization in nitrogen-vacancy centers in diamond nanocrystals, Phys. Rev. B **86**, 045204 (2012).

[37] T. Wolf, P. Neumann, K. Nakamura, H. Sumiya, T. Ohshima, J. Isoya, and J. Wrachtrup, Subpicotesla Diamond Magnetometry, Phys. Rev. X **5**, 041001 (2015).